

A prescription for the asteroseismic surface correction

Yaguang Li (李亚光)^{ID},¹ * Timothy R. Bedding^{ID},¹ † Dennis Stello^{ID},² Daniel Huber^{ID},³
 Marc Hon^{ID},³ Meridith Joyce^{ID},⁴ Tanda Li (李坦达)^{ID},⁵ Jean Perkins^{ID},⁶ Timothy R. White^{ID},¹,
 Joel C. Zinn^{ID},⁷ Andrew W. Howard^{ID},⁸ Howard Isaacson^{ID},⁹ Daniel R. Hey^{ID},³ and Hans Kjeldsen^{ID}¹⁰

¹*Sydney Institute for Astronomy (SIFA), School of Physics, University of Sydney, NSW 2006, Australia*

²*School of Physics, University of New South Wales, 2052, Australia*

³*Institute for Astronomy, University of Hawai'i, 2680 Woodlawn Drive, Honolulu, HI 96822, USA*

⁴*Space Telescope Science Institute, 3700 San Martin Dr, Baltimore, MD 21218, USA*

⁵*Department of Astronomy, Beijing Normal University, Haidian District, Beijing 100875, China*

⁶*Monterey Institute for Research in Astronomy, 200 8th St, Marina, CA 93933*

⁷*Department of Astrophysics, American Museum of Natural History, Central Park West at 79th Street, New York, NY 10024, USA*

⁸*Division of Physics, Mathematics and Astronomy, Caltech, 1200 E California Blvd, Pasadena CA 91125, USA*

⁹*Department of Astronomy, University of California at Berkeley, 501 Campbell Hall, Berkeley, CA 94720-3411, USA*

¹⁰*Stellar Astrophysics Centre, Department of Physics and Astronomy, Aarhus University, 8000 Aarhus C, Denmark*

Accepted XXX. Received YYY; in original form ZZZ

ABSTRACT

In asteroseismology, the surface effect refers to a disparity between the observed and the modelled frequencies in stars with solar-like oscillations. It originates from improper modelling of the surface layers. Correcting the surface effect usually requires using functions with free parameters, which are conventionally fitted to the observed frequencies. On the basis that the correction should vary smoothly across the H–R diagram, we parameterize it as a simple function of surface gravity, effective temperature, and metallicity. We determine this function by fitting a wide range of stars. The absolute amount of the surface correction decreases with luminosity, but the ratio between it and ν_{\max} increases, suggesting the surface effect is more important for red giants than dwarfs. Applying the prescription can eliminate unrealistic surface correction, which improves parameter estimations with stellar modelling. Using two open clusters, we found a reduction of scatter in the model-derived ages for each star in the same cluster. As an important application, we provide a new revision for the $\Delta\nu$ scaling relation that, for the first time, accounts for the surface correction. The values of the correction factor, $f_{\Delta\nu}$, are up to 2% smaller than those determined without the surface effect considered, suggesting decreases of up to 4% in radii and up to 8% in masses when using the asteroseismic scaling relations. This revision brings the asteroseismic properties into an agreement with those determined from eclipsing binaries. The new correction factor and the stellar models with the corrected frequencies are available at <https://www.github.com/parallelpro/surface>.

Key words: stars: solar-type – stars: oscillations (including pulsations) – stars: low-mass

1 INTRODUCTION

Correcting the asteroseismic surface effect has so far been a troublesome procedure. Convection affects pulsation properties through turbulent pressure, opacity variations, and convective energy flux (Houdek et al. 2017). Small-scale magnetic fields can form layers that affect the propagation of pulsations (Li et al. 2021b). All these processes are poorly modelled in the near-surface convective atmosphere in most 1D stellar models (Christensen-Dalsgaard et al. 1988; Dziembowski et al. 1988). Improvements have been seen with the surface

layers replaced by 3D averaged atmospheric models, producing more realistic equilibrium structures (Rosenthal et al. 1999; Magic & Weiss 2016; Jørgensen et al. 2017; Trampedach et al. 2017; Jørgensen et al. 2018, 2019; Mosumgaard et al. 2020), or with time-dependent 1D convection models, accounting for the coupling between oscillation and convection (Balmforth 1992; Grigahcène et al. 2012; Christensen-Dalsgaard 2012; Houdek et al. 2017, 2019; Belkacem et al. 2021; Philidet et al. 2021).

In practice, the surface effect is usually corrected empirically with simple functions of frequency. Christensen-Dalsgaard et al. (1989) provided a justification, based on a perturbation to an asymptotic formalism of acoustic modes.

* yaguang.li@sydney.edu.au

† tim.bedding@sydney.edu.au

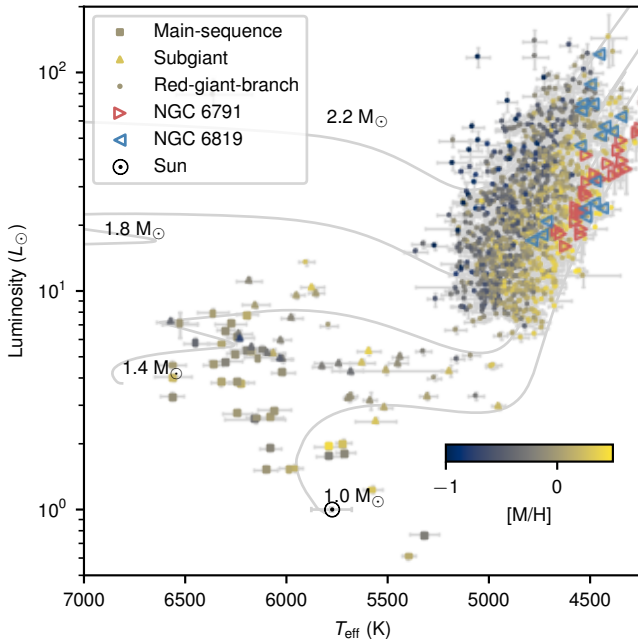


Figure 1. H–R diagram showing the studied sample in this work. The evolutionary tracks for four masses with $Y_{\text{init}} = 0.29$, $[M/H] = 0.0$, $\alpha_{\text{MLT}} = 1.7$ are shown in grey lines. Note these model parameters are approximate, not exact, since the tracks were generated pseudo-randomly (see Sec. 3.2).

By rescaling the frequency correction obtained from the solar standard model, [Silva Aguirre et al. \(2015\)](#) and [Houdek et al. \(2019\)](#) applied it to other main-sequence stars. Several other correction formula were also put forward (e.g. [Kjeldsen et al. 2008](#); [Sonoji et al. 2015](#)). In particular, [Gough \(1990\)](#) suggested that the corrections are proportional to the cubic and the inverse of frequencies scaled by mode inertia:

$$\delta\nu = [a_3(\nu/\nu_{\text{max}})^3 + a_{-1}(\nu/\nu_{\text{max}})^{-1}] / I, \quad (1)$$

where a_3 and a_{-1} are the free parameters to be determined. The frequency of maximum power, ν_{max} , is evaluated via the scaling relation ([Brown et al. 1991](#); [Kjeldsen & Bedding 1995](#)):

$$\frac{\nu_{\text{max}}}{\nu_{\text{max},\odot}} \approx \frac{g}{g_{\odot}} \left(\frac{T_{\text{eff}}}{T_{\text{eff},\odot}} \right)^{-1/2}, \quad (2)$$

where we adopt $g_{\odot} = 274 \text{ m/s}^2$, $T_{\text{eff},\odot} = 5777 \text{ K}$, and $\nu_{\text{max},\odot} = 3090 \mu\text{Hz}$ throughout this work. Since the cubic term usually dominates the frequency correction, another correction form is written as

$$\delta\nu = a_3(\nu/\nu_{\text{max}})^3 / I, \quad (3)$$

where a_3 is the free parameter.

These two functional forms have shown to match observations quite well. [Ball & Gizon \(2014, 2017\)](#) showed that they work well for radial modes on the Sun and red-giant-branch stars, albeit with some caveats for mixed modes ([Ong et al. 2021a,b](#)). Many works concluded the inverse-cubic form could obtain an overall good fit ([Schmitt & Basu 2015](#); [Compton et al. 2018](#); [Nsamba et al. 2018](#); [Jørgensen et al. 2020](#)) and correctly recover the dynamical stellar properties of binary systems ([Jørgensen et al. 2020](#)).

The correction usually works as follows. Given a star with a set of observational frequencies and a stellar model with a set of theoretical frequencies, one can calculate the difference between the two frequency sets. This difference is then fitted to the right-hand-side of the frequency correction function (Eq. 1 or 3) to determine the free parameters. The amount of frequency correction is then calculated with the best-fitting values and added to the theoretical frequencies.

One problem with this method is that the surface correction can only be determined with a fit to observed frequencies. It does not allow us to estimate the surface terms for any theoretical model without being close to the observed star. More seriously, it can lead to a model with an unphysically large (or small) surface correction that fits the data well but is a poor representation of the star. In this paper, we tackle these problems through a simple prescription for the surface effect, assuming that it varies smoothly with stellar parameters (Sec. 2). This variation is then constrained by an ensemble fit to a wide range of stars (Sec. 3). Adopting this prescription improves parameter estimations with stellar modelling (Sec. 4). It further enables an improved correction to the commonly-used $\Delta\nu$ scaling relation (Sec. 5).

2 PRESCRIBING THE SURFACE CORRECTION

Since the surface effect originates from the model atmosphere, it is reasonable to assume it is a smooth function of surface parameters, i.e. surface gravity g , effective temperature T_{eff} , and metallicity $[M/H]$. This assumption is supported by 3D atmospheric simulations ([Sonoji et al. 2015](#); [Manchon et al. 2018](#)) and 1D non-adiabatic convection models ([Houdek et al. 2019](#)). These works suggested that the surface correction at ν_{max} , denoted by $\delta\nu_{\text{m}}$, varies from star to star as a function of T_{eff} and g . Hence, we propose a prescription for $\delta\nu_{\text{m}}$ as follows:

$$\delta\nu_{\text{m}} = a \cdot (g/g_{\odot})^b \cdot (T_{\text{eff}}/T_{\text{eff},\odot})^c \cdot (d \cdot [M/H] + 1), \quad (4)$$

where the free parameters to be determined are $\theta_s = \{a, b, c, d\}$. By construction, the parameter a is the amount of surface correction at ν_{max} for a solar model. If we adopt the cubic formula, for each star we can directly use Eq. 4 to solve the surface term a_3 in Eq. 3 with ν equal to ν_{max} . To obtain the mode inertia I on the RHS of Eq. 3, we interpolated ν^3/I to the frequency ν_{max} .

If we adopt the inverse-cubic formula to correct model frequencies, another equation is needed since there are two surface terms, a_{-1} and a_3 . We propose that the surface correction at s times of ν_{max} , denoted by $\delta\nu'_{\text{m}}$, also varies with the surface parameters:

$$\delta\nu'_{\text{m}} = a' \cdot (g/g_{\odot})^{b'} \cdot (T_{\text{eff}}/T_{\text{eff},\odot})^{c'} \cdot (d' \cdot [M/H] + 1). \quad (5)$$

Together with Eq. 4, the free parameters in this prescription are $\theta_s = \{a, b, c, d, a', b', c', d'\}$. By varying the value of s , we found no obvious changes to the solutions of those free parameters. Hence, we fixed s at 1.1, so that $\delta\nu'_{\text{m}}$ represents the amount of surface correction at $1.1\nu_{\text{max}}$. For each star, we then used Eq. 4 and Eq. 5 to solve a_{-1} and a_3 in Eq. 1 with $\nu = \nu_{\text{max}}$ and $\nu = 1.1\nu_{\text{max}}$, respectively. To calculate the RHS of Eq. 1, we interpolated ν^3/I and ν^{-1}/I to the frequency ν_{max} .

Table 1. Stellar parameters of the studied sample.

Star	L	σ_L	Ref(L)	T_{eff}	$\sigma_{T_{\text{eff}}}$	Ref(T_{eff})	[M/H]	$\sigma_{\text{[M/H]}}$	Ref([M/H])
Sun	1.0	0.02	—	5777	100	—	0.0	0.05	—
μ Her	2.54	0.08	2	5560	100	3	0.28	0.05	3
KIC10000547	12.68	0.51	0	4969	36	1	-0.26	0.05	6
KIC10001440	39.77	3.8	0	4773	42	1	-0.65	0.05	6
KIC10004825	42.35	3.34	0	4611	55	1	0.21	0.05	6
KIC10014893	68.69	4.67	0	4579	26	1	-0.13	0.05	6
KIC10014959	9.29	0.33	0	4813	29	1	0.11	0.05	6
KIC10018442	37.7	1.89	0	4781	41	1	-0.03	0.05	6
KIC10018811	27.11	1.41	0	4918	28	1	-0.29	0.05	6

Note: References for the stellar parameters: 0 (This work); 1 (Casagrande et al. 2021); 2 (Grundahl et al. 2017); 3 (Jofré et al. 2015); 4 (Furlan et al. 2018); 5 (Lund et al. 2017); 6 (Ahumada et al. 2020); 7 (Buchhave & Latham 2015). Only the first 10 lines are shown. The full table can be accessed online.

3 DATA ANALYSIS

3.1 Observational sample

In order to constrain Eqs. 4 and 5, we need a sample of stars spanning a sufficiently large parameter space. Our sample (see Fig. 1) consists of stars with measured individual frequencies: the Sun (Broomhall et al. 2009), the SONG subgiant μ Herculis (Grundahl et al. 2017), *Kepler* main-sequence dwarfs (Lund et al. 2017), *Kepler* subgiants (Li et al. 2020a) and *Kepler* red-giant-branch (RGB) stars with $\Delta\nu > 2 \mu\text{Hz}$ (Li et al. 2022). The RGB stars were distinguished from helium-burning stars by Bedding et al. (2011), Stello et al. (2013), Mosser et al. (2014), Vradar et al. (2016), Elsworth et al. (2017), and Hon et al. (2017).

We compiled metallicities [M/H] from various sources, including HIRES spectra (see below), APOGEE DR16 (Ahumada et al. 2020), Lund et al. (2017), and Buchhave & Latham (2015) (listed in the order of priority) wherever possible. We collected metallicities for 36 stars measured with HIRES spectrograph (Vogt et al. 1994) at the Keck-I 10-m telescope on Maunakea observatory, Hawai‘i by Furlan et al. (2018). We also obtained new HIRES spectra for 21 stars in this work. The spectra were obtained and reduced as part of the California Planet Search queue (CPS, Howard et al. 2010). We used the C5 decker and obtained spectra with a S/N per pixel of 80 at $\sim 600 \text{ nm}$ with a spectral resolving power of $R \sim 60000$. To measure the metallicities, we applied Specmatch-synth (Petigura 2015), which fits a synthetic grid of model atmospheres and has been extensively validated through the California Kepler Survey (Petigura et al. 2017; Johnson et al. 2017). All metallicity measurements were brought to the APOGEE abundance scale by adding constant offsets, determined with the [M/H] measurements of same stars. Because of the limited number of metal-poor stars, we restricted our sample to have [M/H] $> -0.8 \text{ dex}$.

We determined the effective temperatures, T_{eff} , with *Gaia* and 2MASS photometry, using the infrared flux method (IRFM) calibrated by Casagrande et al. (2021). This T_{eff} scale was benchmarked against solar twins, *Gaia* benchmark stars, and interferometry.

We determined luminosities, L , using *Gaia* DR3 (Gaia Collaboration et al. 2016, 2021). *Gaia* parallaxes are known to have zero-point offsets, which we corrected using a model from Lindegren et al. (2021). The reported parallaxes also have underestimated uncertainties. Therefore we inflated them by a factor of 1.3, according to external calibrations

(El-Badry et al. 2021; Zinn 2021; Maíz Apellániz et al. 2021). We then calculated the luminosities by combining the parallaxes with the 2MASS K -band magnitudes and using the “direct” method in the software ISOCCLASSIFY (Huber et al. 2017; Berger et al. 2020), which implements the Green et al. (2019) dust map and the bolometric corrections from MIST models (Choi et al. 2016).

Additionally, we used RGB stars from two *Kepler* clusters as a test sample: NGC 6791 (Basu et al. 2011; McKeever et al. 2019; Brogaard et al. 2021) and NGC 6819 (Stello et al. 2010; Corsaro et al. 2012; Handberg et al. 2017). These cluster stars were not used for fitting the prescription, but for validating the result (Sec. 4). We estimated their stellar parameters following the same procedure illustrated above. Table 1 lists the stellar parameters used in modelling. Fig. 1 shows an overview of our sample on the H–R diagram.

3.2 Stellar models

We calculated a grid of stellar models using Modules for Experiments in Stellar Astrophysics (MESA, version r15140; Paxton et al. 2011, 2013, 2015, 2018, 2019) to model stellar evolution and structure, and GYRE (version 6.0.1; Townsend & Teitler 2013) to calculate adiabatic frequencies from the structure profiles computed from MESA.

Here, we summarise the input physics for the constructed models. We used the Henyey et al. (1965) description of the mixing length theory to formulate convection, with the mixing length being one of the free parameters, since a solar-calibrated mixing length can not fit stars with various stellar properties (Tayar et al. 2017; Joyce & Chaboyer 2018a). We set the convective overshoot with an exponential scheme discussed by Herwig (2000). For core overshoot, we set the efficiency parameter $f_{\text{ov,core}}$ as a function of mass, according to the calibration from eclipsing binaries (equation 2 of Claret & Torres 2018). For envelope overshoot, we set $f_{\text{ov,env}}$ as 0.006, according to a solar calibration with our adopted input physics.

We chose the current solar photospheric abundance as the reference scale for metallicity: $X_{\odot} = 0.7381$, $Y_{\odot} = 0.2485$, $Z_{\odot} = 0.0134$ (Asplund et al. 2009, the AGSS09 scale). Hence the metallicity is

$$[\text{M}/\text{H}] = \log_{10}(Z/X) - \log_{10}(Z_{\odot}/X_{\odot}). \quad (6)$$

The opacity tables were accordingly chosen based on the

AGSS09 metal mixture. MESA implements electron conduction opacities (Cassisi et al. 2007) and radiative opacities from OPAL (Iglesias & Rogers 1993, 1996), except low-temperature data (Ferguson et al. 2005) and the high-temperature Compton-scattering regime (Buchler & Yueh 1976). The equation of state adopted by MESA blends from OPAL (Rogers & Nayfonov 2002), SCVH (Saumon et al. 1995), PTEH (Pols et al. 1995), HELM (Timmes & Swesty 2000), and PC (Potekhin & Chabrier 2010). We adopted nuclear reaction rates from JINA REACLIB database. We only considered a minimal set of elements specified in `basic.net` of MESA. We did not account for atomic diffusion or gravitational settling in the models.

For the surface boundary conditions, we used the grey model atmosphere together with Eddington $T - \tau$ integration (Eddington 1926). We caution that by default, MESA does not include the atmosphere in the output structure. The resulting bias looks very similar to the surface effect, although the amount of correction is larger. To avoid this, one should specifically set `add_atmosphere_to_pulse_data` as `.true`.

The free parameters for the model grid are stellar mass $M \in (0.7, 2.3) M_{\odot}$, initial helium abundance $Y_{\text{init}} \in (0.22, 0.32)$, metallicity $[M/H] \in (-0.94, 0.56)$ (the corresponding Z_{init} ranges from 0.0016 to 0.0522), and mixing-length parameter $\alpha_{\text{MLT}} \in (1.3, 2.7)$. These four parameters were uniformly sampled in a quasi-random Sobol sequence with a total number of 8191 (Bellinger et al. 2016). Each set of parameters uniquely determines an evolutionary track. Along each evolutionary track, we saved one structure model at least every 0.3 μHz in $\Delta\nu$ or 5 K in T_{eff} . For each structure model, we calculated radial mode frequencies with GYRE in a wide frequency range around ν_{max} . We used the 6th-order Gauss-Legendre Magnus method to solve the adiabatic oscillations. We caution that a lower-order algorithm could produce inaccurate frequencies, which differ by an amount larger than the typical observational uncertainties. Although a higher-order scheme is sensitive to abrupt changes in the structure, we examined the variables (such as density, temperature, sound speed and the first adiabatic index) in the set of oscillation equations, and found they vary smoothly near the atmospheres.

3.3 Fitting method

We now describe the fitting method to obtain the surface parameters θ_s in the prescriptions. They determine the amount of surface correction of each model $\theta_m = \{M, Y_{\text{init}}, \alpha_{\text{MLT}}, [M/H], \text{age}\}$. For each star i , we considered three classical constraints $q = \{L, T_{\text{eff}}, [M/H]\}$ (e.g. Valle et al. 2015; Joyce & Chaboyer 2018b; Duan et al. 2021; Jiang & Gizon 2021):

$$\chi_{\text{classical},i}^2 = \sum_q \frac{(q_{\text{mod},i} - q_{\text{obs},i})^2}{\sigma_{q,i}^2}. \quad (7)$$

The seismic constraints include radial mode frequencies. They are normalised by the number of observed modes N_i , in order to avoid unrealistically small error bars (Cunha et al. 2021; Aguirre Borsen-Koch et al. 2022):

$$\chi_{\text{seismic},i}^2 = \frac{1}{N_i} \sum_n \frac{(\nu_{\text{mod},n,i} + \delta\nu_{n,i} - \nu_{\text{obs},n,i})^2}{\sigma_{\text{mod}}^2 + \sigma_{\text{obs},n,i}^2}. \quad (8)$$

Normalising by the number of modes N_i in $\chi_{\text{seismic},i}^2$ is equivalent to reducing the relative weight of $\chi_{\text{seismic},i}^2$ with respect to $\chi_{\text{classical},i}^2$ and artificially inflating returned formal uncertainties. Cunha et al. (2021) noted that this is a common practice in stellar modelling, but it is not statistically valid and is sometimes unable to capture the systematic uncertainties originating from stellar physics. In the above equation, $\delta\nu_{n,i}$ is the amount of surface correction, and σ_{mod} is the systematic uncertainty of stellar model frequencies (Li et al. 2020b; Ong et al. 2021b). To evaluate σ_{mod} , we identified the best-fitting model (using the above χ_{seismic}^2 and treating $\sigma_{\text{mod},i}$ as 0) and calculated its root-mean-square difference between the observed and corrected modelled frequencies. At this step, the amount of surface correction for each mode, $\delta\nu_{n,i}$, was determined by fitting Eq. 1 or 3 to the actual differences between the uncorrected model frequencies $\nu_{\text{mod},n,i}$ and the observed frequencies $\nu_{\text{obs},n,i}$ (i.e. the traditional star-by-star surface correction). We then fitted the root-mean-square differences as a function of ν_{max} and T_{eff} for the whole sample and used this function to describe σ_{mod} , which gave

$$\sigma_{\text{mod}}/\mu\text{Hz} = 1.65 \cdot (\nu_{\text{max}}/\nu_{\text{max},\odot})^{1.45} (T_{\text{eff}}/T_{\text{eff},\odot})^{2.30}. \quad (9)$$

The value of σ_{mod} is generally smaller than σ_{obs} in RGB stars and comparable in main-sequence stars, hence the poorly- and well-observed modes in one star are not weighted similarly. For our final fitting, $\delta\nu_{n,i}$ was calculated using the prescription described in Sec. 2.

To obtain the probability distributions of the surface parameters θ_s , we marginalised the probability over other model parameters:

$$p_i(\theta_s) = \int \exp[-(\chi_{\text{classical},i}^2 + \chi_{\text{seismic},i}^2)/2] d\theta_m. \quad (10)$$

Since θ_m is sampled on a pre-computed model grid, in practice, we approximated this integration by taking the average values of the integrated function for all eligible models. Finally, putting them together, we maximised the joint probability from all stars in the sample:

$$p(\theta_s) = \prod_i p_i(\theta_s) \quad (11)$$

We used a gradient descent algorithm written with JAX and OPJAX (Babuschkin et al. 2020) to optimise this function. We adopted the uncertainties for the fitted parameters using the diagonal elements of the covariance matrix, which was constructed with the Hessian matrix for $\log p$. Ensemble modelling to constrain uncertain stellar physics has been used to study the mixing length and helium abundance (Lyttle et al. 2021).

3.4 Fitting results

In addition to fitting the whole sample, we performed fits in two classes of stars: pre-RGB ($\nu_{\text{max}} > 283 \mu\text{Hz}$) and RGB ($\nu_{\text{max}} < 283 \mu\text{Hz}$). In Table 2, we show the best-fitting values of the surface parameters in the prescriptions. Firstly, the best-fitting parameters for the whole sample and the RGB sample are similar, since RGB stars dominate the sample. Secondly, the power indices for g , T_{eff} , and $[M/H]$ (b , c , and d) are quite different for the RGB fit compared to the pre-RGB fit. These parameters are also highly correlated, indicating that their values could be poorly constrained, rather than highly

Table 2. Best-fitting parameters in the surface correction prescriptions. The stellar models are calculated with $T - \tau$ integrated model atmospheres using the Eddington relation.

Atmosphere Model	Sample	a	b	c	d	a'	b'	c'	d'
Eddington Cubic	All	-4.15 ± 0.13	0.95 ± 0.01	-5.48 ± 0.23	-1.10 ± 0.03	—	—	—	—
Eddington Cubic	Pre-RGB	-4.19 ± 0.39	0.78 ± 0.07	-5.71 ± 0.58	-0.07 ± 0.13	—	—	—	—
Eddington Cubic	RGB	-4.18 ± 0.13	0.96 ± 0.01	-5.64 ± 0.22	-1.11 ± 0.02	—	—	—	—
Eddington Inverse-cubic	All	-3.74 ± 0.13	1.09 ± 0.01	-8.74 ± 0.23	-1.38 ± 0.02	-4.99 ± 0.14	1.05 ± 0.01	-8.15 ± 0.18	-1.32 ± 0.02
Eddington Inverse-cubic	Pre-RGB	-3.72 ± 0.40	0.61 ± 0.08	-1.68 ± 0.82	-0.08 ± 0.14	-5.55 ± 0.42	0.65 ± 0.06	-1.57 ± 0.62	-0.65 ± 0.11
Eddington Inverse-cubic	RGB	-3.84 ± 0.16	1.10 ± 0.01	-8.83 ± 0.24	-1.38 ± 0.02	-5.04 ± 0.17	1.07 ± 0.01	-8.33 ± 0.19	-1.33 ± 0.02

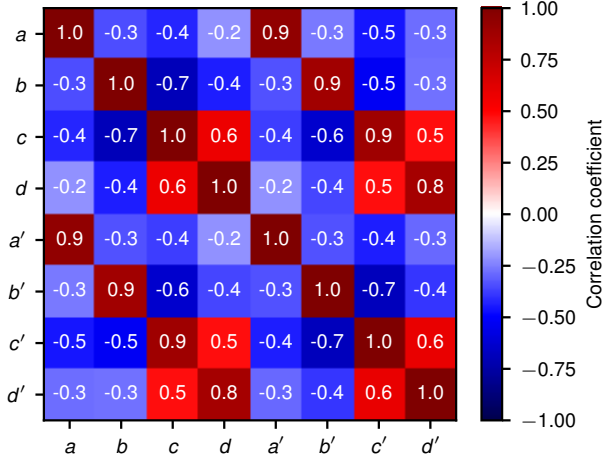


Figure 2. Correlation matrix of the fitted parameters for the full sample using the inverse-cubic model.

physically different. Fig. 2 shows the correlation matrix of the fitted parameters for the full sample using the inverse-cubic model. Thirdly, although the reported uncertainties are small, we observed strong correlations (correlation coefficient greater than 0.5) between b and c , b' and c' , c and d , c' and d' , a and a' , b and b' , c and c' , and d and d' . Fourthly, the inverse-cubic and the cubic models show little differences. We discuss the inverse-cubic model and the fit with the whole sample in the rest of the paper.

To visualise our fitting result, we colour-coded the values of $\delta\nu_m$ and $\delta\nu_m/\nu_{\max}$ in Fig. 3 on the $\Delta\nu$ - T_{eff} diagrams. In terms of the absolute value $\delta\nu_m$ (which is always negative), the main-sequence stars have the largest amount of surface correction. It decreases towards higher T_{eff} (hotter F-stars) and smaller $\Delta\nu$ (more luminous red giants). Concerning the relative value of $\delta\nu_m$ with respect to ν_{\max} , the trend is reversed. The main-sequences stars have smaller corrections, and the surface effect becomes increasingly significant for luminous red giants. Those trends are similar compared to those found by Trampedach et al. (2017, Fig. 5 and 6), who improved the mean atmospheric structure with 3D-averaged models (the so-called “structural effect”).

Sonoi et al. (2015, Eqs. 9 and 10) also studied the structural effect, mainly for dwarfs and subgiants, and concluded positive correlations between $\delta\nu_m$ and g or T_{eff} . Houdek et al. (2019, Fig. 5) studied the “modal effect”, which accounts for the coupling between convection and oscillation, and reported a similar correlation with their 1D time-dependent convec-

tion models. These works are qualitatively consistent with our best-fitting parameters for dwarfs and subgiants (Table 2).

We emphasise that the values reported in Table 2 may not be directly applicable to other stellar models, which could have different outer boundary conditions. For example, in Fig. 2 of Christensen-Dalsgaard et al. (1996) there are three modifications to the solar atmosphere: one with an alternative treatment of the convective flux, one with the inclusion of turbulent pressure, and one with replacement from 3D averaged models. Each one has a different value for the surface effect at ν_{\max} , ranging from 5 to 17 μHz , suggesting that an alternative atmosphere could differ by a factor of three from our fitted values for the Sun. Moreover, the differences in the model physics and even numerical treatment can change the fitted values. To test this, we applied our prescriptions to a grid of models calculated by Sharma et al. (2016). Even though they set the same Eddington atmosphere with MESA as in this work, we obtained unrealistically large corrections in their models at high radial orders. Additionally, Appendix A examines an alternative atmosphere based on the Hopf $T - \tau$ relation. We found that the fitted coefficients are drastically different from those obtained using the Eddington relation. Hence, to correctly implement our method, we recommend to either use the stellar models corrected in this work or to re-fit the prescriptions with stellar models of the user’s choice.

4 IMPROVEMENTS ON PARAMETER ESTIMATIONS

We now check whether applying our prescription introduces bias in the estimated stellar properties. In Fig. 4, we show the fractional differences of mass, radius, and age, between modelling without and with the prescription. The differences have medians fluctuating around 0, suggesting no systematic bias.

Next, we demonstrate two major improvements by using our method. Firstly, we note that adopting the prescriptions reduces outliers when inferring parameters from stellar modelling. For example, Fig. 4 shows some stars significantly away from the median values. These data points correspond to a poor fit due to the unconstrained surface correction. To confirm this, we show the differences between the modelled and observed values of $\Delta\nu$ in Fig. 5, where the former were obtained from the best-fitting model. The model $\Delta\nu$ values were determined from the slope of a linear fit to the radial frequencies versus the orders, with weights of each mode assigned by a Gaussian envelope (centred around ν_{\max} ; see White et al. 2011)

$$w = \exp \left[-\frac{(\nu - \nu_{\max})^2}{2\sigma^2} \right], \quad (12)$$

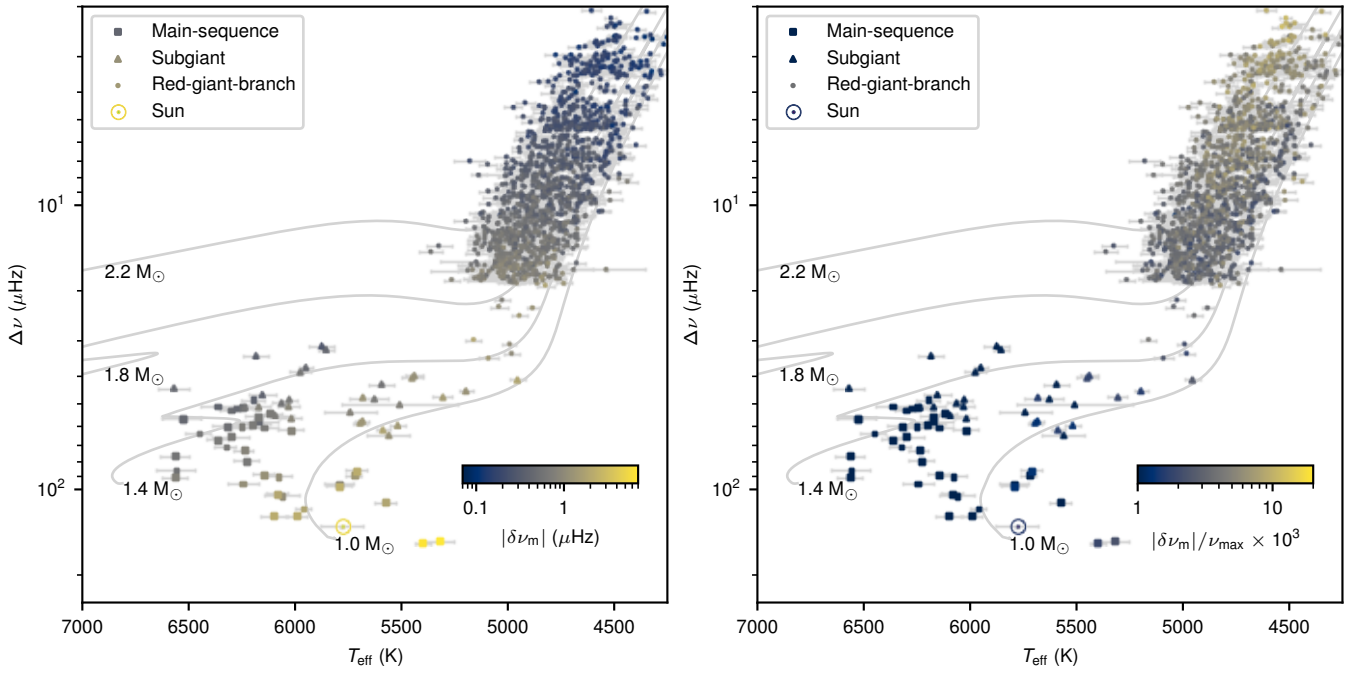


Figure 3. Surface correction at ν_{\max} , $\delta\nu_m$, determined based on the prescriptions with the inverse-cubic model, shown on the $\Delta\nu$ - T_{eff} diagrams. The left panel colour-codes the absolute value of $\delta\nu_m$ (which is negative). The right panel colour-codes the dimensionless quantity, $\delta\nu_m/\nu_{\max}$. The $M = 1.0, 1.4, 1.8$ and $2.2 M_{\odot}$ evolutionary tracks are shown in grey lines.

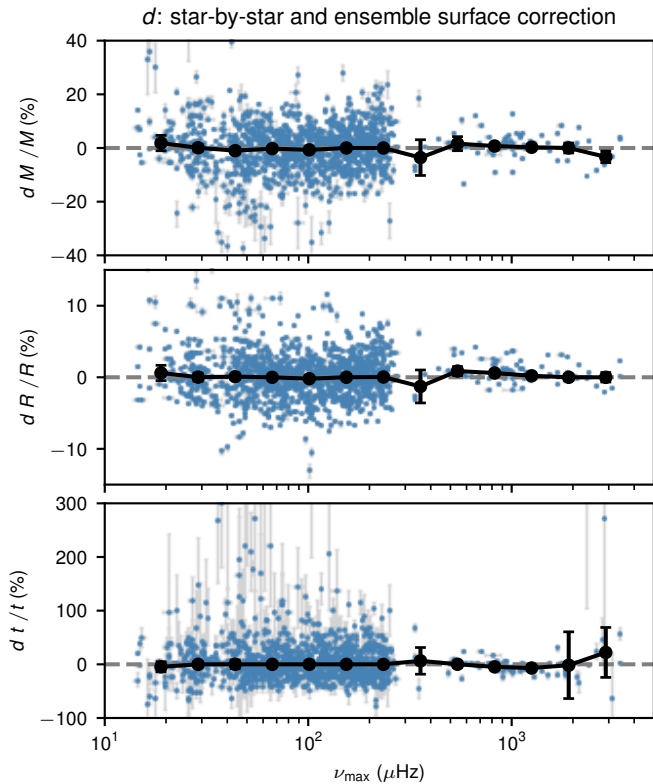


Figure 4. Fractional differences of mass, radius, and age, between modelling using star-by-star and ensemble surface correction. The medians and the associated error bars in bins of equal width in $\log \nu_{\max}$ are shown in black circles.

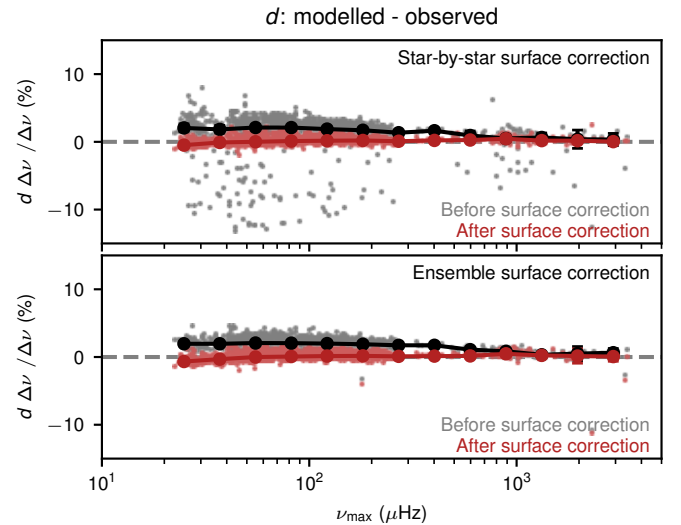


Figure 5. Fractional differences of theoretical and observational $\Delta\nu$. The top panel shows results from star-by-star fits. The bottom panel shows those from ensemble fits.

where $\ln \sigma/\mu\text{Hz} = 0.964 \ln \nu_{\max}/\mu\text{Hz} - 1.715$, which was estimated based on a fit to observations (Yu et al. 2018; Lund et al. 2017; Li et al. 2020a). The values are similar to those obtained by Mosser et al. (2012). For all models in this work, we calculated the modes within 5σ of ν_{\max} .

By comparing the red points in the two panels, we noticed that the differences are similar after the surface correction, independent of whether using the prescription or not. This is expected, since the corrected frequencies were constructed to

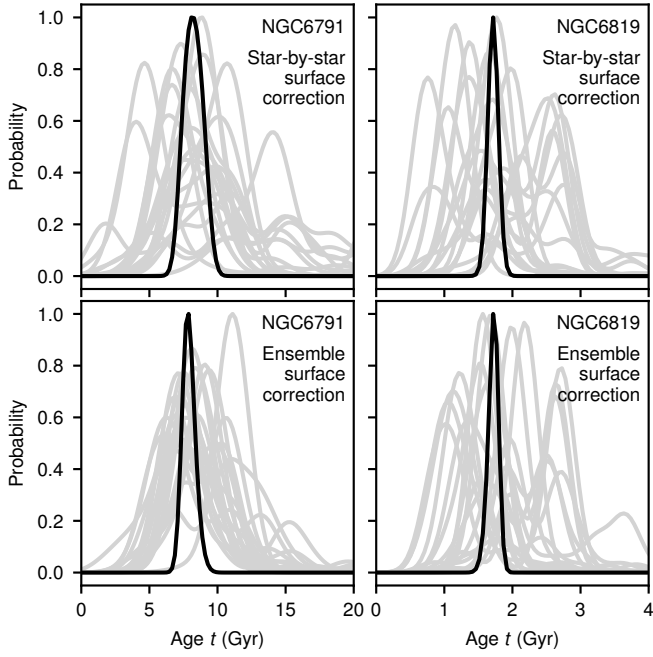


Figure 6. Probability distributions of stellar ages for the RGB stars within the *Kepler* open clusters NGC 6791 and NGC 6819. The age probability for each star are shown in grey, while the joint probability distribution is shown in black. Modelling with the prescription (lower panels) shows a reduction of the scatter in age, compared to modelling with a star-by-star surface correction (upper panels).

fit with the observed frequencies. However, when we compare the grey points in both panels, which represent $\Delta\nu$ calculated from the uncorrected frequencies, the outliers are only present in the case of star-by-star fit (top panel). These outliers are eliminated when the prescription was applied in the ensemble fit (bottom panel).

Secondly, we argue that adopting the prescriptions also reduces scatter in model-based parameters. This can be seen from modelling stars in open clusters, members of which are expected to have the same age. We examined the test sample introduced in Sec. 3.1, namely the RGB stars in NGC 6791 and NGC 6819. In Fig. 6, we show the probability distributions of ages for each star (in grey lines), and compare them with and without using our new prescription. It is evident that the probabilities with the prescriptions applied display smaller scatter overall. The root-mean-square values of individual model-based ages reduces from 2.11 Gyr to 1.60 Gyr for NGC 6791, and from 0.46 Gyr to 0.34 Gyr for NGC 6819.

On a side note, we compared our age estimates for the two open clusters against recent studies in Table 3. Our estimates occupy the lower end of the published ages. We attribute this to our adopted observational constraints: the relatively high metallicity for NGC 6791 ($[M/H] = 0.36$ dex), and the large extinction value for NGC 6819 (mean $E(B - V) = 0.17$). The effect of extinction and metallicity on age can be seen from Table 2 of Basu et al. (2011).

To allow easy-access to our stellar models and the surface-corrected frequencies, we published them in an online repository (see Data Availability).

Table 3. List of ages for the two open clusters.

Age (Gyr)	Methods	References
NGC 6791		
6.8 – 8.6	Seismology	Basu et al. (2011)
7.68 ± 1.60	Seismology	This work
8.2 ± 0.3	Seismology	McKeever et al. (2019)
8.3 ± 0.8	Isochrone fitting	Brogaard et al. (2012)
8.3	Binary	Brogaard et al. (2021)
10.1 ± 0.9	Seismology	Kallinger et al. (2018)
NGC 6819		
1.57 ± 0.34	Seismology	This work
2 – 2.4	Seismology	Basu et al. (2011)
2.4	Isochrone fitting	Jeffries et al. (2013)
2.4 ± 0.2	Eclipsing binary	Brewer et al. (2016)
2.5	Isochrone fitting	Balona et al. (2013)
2.62 ± 0.25	Eclipsing binary	Sandquist et al. (2013)
2.9 ± 0.3	Seismology	Kallinger et al. (2018)
3.1 ± 0.4	Eclipsing binary	Jeffries et al. (2013)

5 CORRECTION TO THE P-MODE LARGE SEPARATION FROM STELLAR MODELS

The scaling relation that relates the p-mode large separation $\Delta\nu$ to stellar mean density, $\Delta\nu \propto \sqrt{\rho}$ (Ulrich 1986), is broadly used (see Hekker 2020, for a review). This relation is only an approximation and stellar models have been used to correct it (White et al. 2011; Sharma et al. 2016; Guggenberger et al. 2016; Rodrigues et al. 2017; Serenelli et al. 2017; Pinsonneault et al. 2018). Sharma et al. (2016, hereafter S16) introduced a correction factor $f_{\Delta\nu}$ to the standard $\Delta\nu$ scaling relation:

$$\left(\frac{\Delta\nu}{\Delta\nu_{\odot}}\right) = f_{\Delta\nu} \left(\frac{\rho}{\rho_{\odot}}\right)^{0.5}, \quad (13)$$

where $\Delta\nu_{\odot} = 135.1 \mu\text{Hz}$ is the solar value of the large frequency separation (Huber et al. 2011).

The correction factor $f_{\Delta\nu}$ are used when estimating the mass and radius via the usual scaling relations (Stello et al. 2008; Kallinger et al. 2010):

$$\frac{M}{M_{\odot}} \approx \left(\frac{\nu_{\max}}{\nu_{\max,\odot}}\right)^3 \left(\frac{\Delta\nu}{f_{\Delta\nu}\Delta\nu_{\odot}}\right)^{-4} \left(\frac{T_{\text{eff}}}{T_{\text{eff},\odot}}\right)^{3/2}, \quad (14)$$

and

$$\frac{R}{R_{\odot}} \approx \left(\frac{\nu_{\max}}{\nu_{\max,\odot}}\right) \left(\frac{\Delta\nu}{f_{\Delta\nu}\Delta\nu_{\odot}}\right)^{-2} \left(\frac{T_{\text{eff}}}{T_{\text{eff},\odot}}\right)^{1/2}. \quad (15)$$

To use Eq. 13 to determine $f_{\Delta\nu}$ from models, we need to know the model-predicted density and $\Delta\nu$, the latter of which is usually calculated from radial oscillation frequencies. Since the surface correction is negative, we expect that the model $\Delta\nu$ value will decrease when the correction is applied (Kjeldsen et al. 2008). However, this correction was previously ignored. Here, we investigate this change and analyse its implication on stellar properties derived from the asteroseismic relations.

5.1 Results

Firstly, we present the correction factor, $f_{\Delta\nu}$, calculated from our stellar models and prescriptions. Fig. 7 shows $f_{\Delta\nu}$ as a function of T_{eff} (left panels) and $\Delta\nu$ (right panels), for three

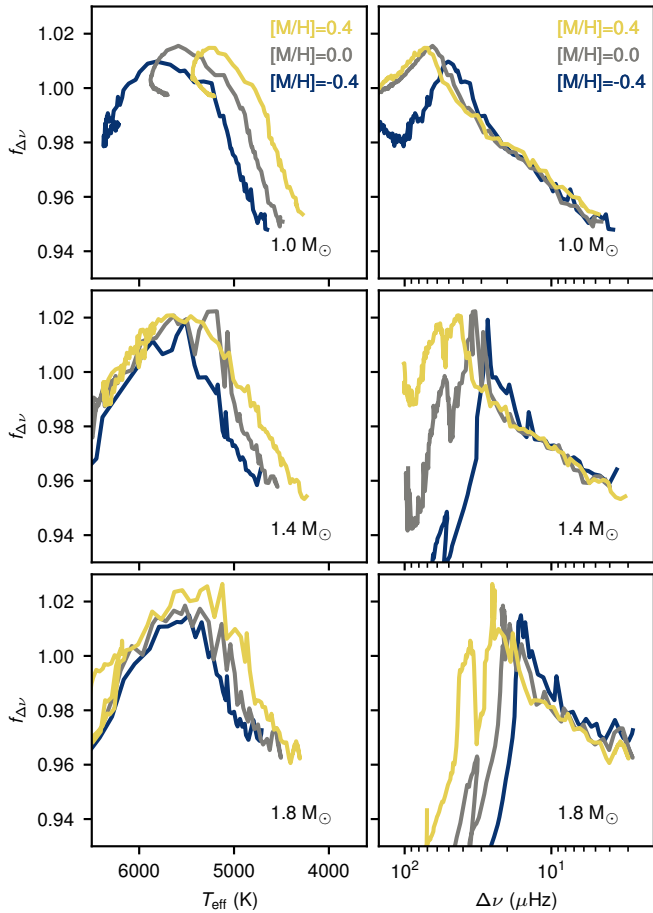


Figure 7. Correction factor for the $\Delta\nu$ scaling relation, $f_{\Delta\nu}$, as a function of T_{eff} (left panels) and $\Delta\nu$ (right panels) for three metallicities and three masses. The values for $f_{\Delta\nu}$ were derived using stellar models with the surface correction considered. The small fluctuations along the lines arise from the uncertainty in the helium abundance and the mixing length parameter.

masses and three metallicities. The overall variations of $f_{\Delta\nu}$ resemble those calculated from models by [White et al. \(2011, Fig. 4\)](#) and [S16 \(Fig. 4\)](#), neither of which included a surface correction. However, our values for $f_{\Delta\nu}$ are systematically smaller compared to the work from [S16](#), due to this correction. [Fig. 8](#) shows the effect of surface correction on $f_{\Delta\nu}$. The change of $f_{\Delta\nu}$ is small for main-sequence stars, but is larger on the RGB, showing an $\sim 2\%$ reduction, where the surface correction is relatively significant (see also [Fig. 3b](#)).

The revised correction factors can be used to estimate the mass and radius via [Eq. 14](#) and [15](#). Unlike the surface corrections done in [Sec. 3.3](#), these do not require any additional model calculations by the user. They simply involve revising the standard scaling relation. We provide a Python routine to derive $f_{\Delta\nu}$ given user-specified observables, based on the models that are calibrated in this work. For a given star, the user specifies observational constraints and their associated uncertainties (e.g. L , T_{eff} , $[M/H]$ and ν_{max}). Each model is assigned with a χ^2 (using [Eq. 7](#)). Next, the correction factor $f_{\Delta\nu}$ of the star is estimated by taking the average of model $f_{\Delta\nu}$ values, weighted by $\exp(-\chi^2/2)$.

We can also provide a simple fitting formula of $f_{\Delta\nu}$ with

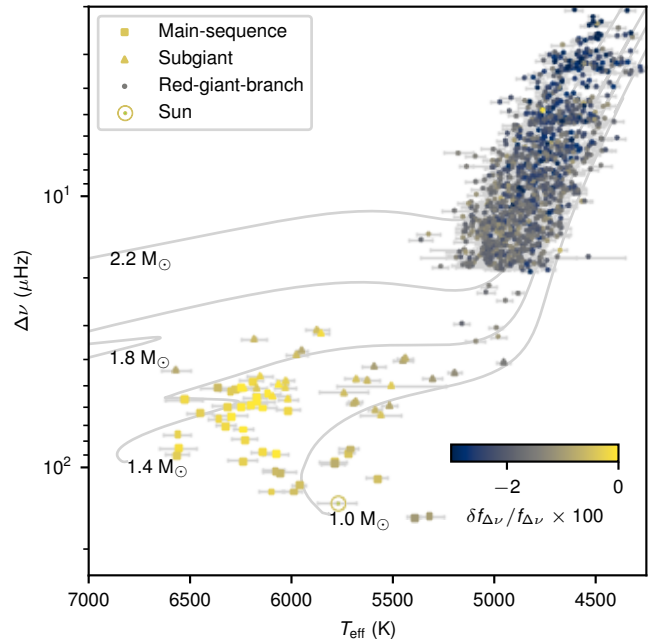


Figure 8. Fractional differences of $f_{\Delta\nu}$ between before and after the surface correction.

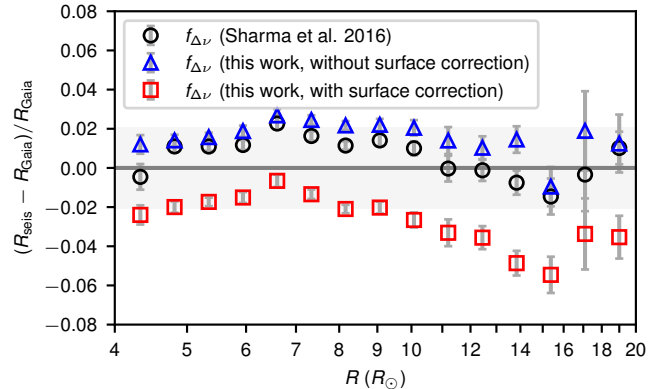


Figure 9. Comparison of *Gaia* radii and asteroseismic radii, using $f_{\Delta\nu}$ calculated in [S16](#) and this work. The data points are binned medians, and the error bars represent the standard errors of the medians. The grey band highlights the 2% systematic uncertainties (e.g. temperature scale) discussed by [Zinn et al. \(2019\)](#).

respect to stellar properties. We explored various functional forms (linear, log-linear and polynomial) and included the observed ν_{max} , $\Delta\nu$, T_{eff} and $[M/H]$ as independent variables to perform simple regressions. The following form obtains a reasonably good fit ($r^2 = 0.85$) and avoids over-fitting with

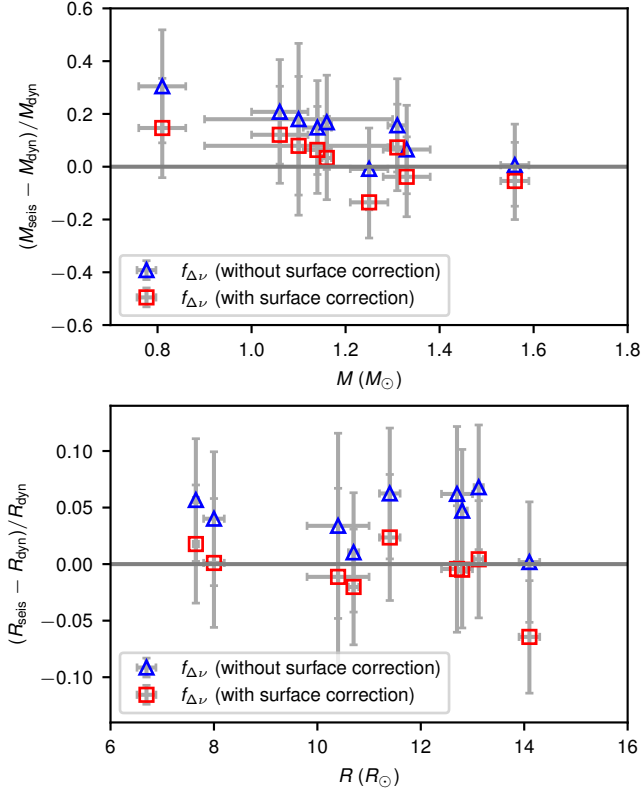


Figure 10. Comparison of the dynamical and the asteroseismic masses and radii using eclipsing binaries (Gaulme et al. 2016; Themeßl et al. 2018; Brogaard et al. 2018; Benbakoura et al. 2021). The asteroseismic properties were determined using $f_{\Delta\nu}$ with and without the surface correction, respectively.

higher orders (examined via cross-validation):

$$\begin{aligned}
 f_{\Delta\nu} = & \beta_0 + \beta_1 \log_{10}(\nu_{\max}/3090 \text{ } \mu\text{Hz}) \\
 & + \beta_2 \log_{10}(\Delta\nu/135.1 \text{ } \mu\text{Hz}) \\
 & + \beta_3(T_{\text{eff}}/5777 \text{ K}) \\
 & + \beta_4(T_{\text{eff}}/5777 \text{ K})^2 \\
 & + \beta_5(T_{\text{eff}}/5777 \text{ K})^3 \\
 & + \beta_6[\text{M}/\text{H}], \\
 & \text{for } 0.8 < M/M_{\odot} < 2.2, \quad -0.8 < [\text{M}/\text{H}] < 0.5, \\
 & \text{and pre-RGB tip } (\Delta\nu > 2.0 \text{ } \mu\text{Hz}).
 \end{aligned} \tag{16}$$

The best-fitting parameters are $\beta = \{4.015 \pm 0.225, 0.168 \pm 0.012, -0.186 \pm 0.015, -10.234 \pm 0.735, 11.432 \pm 0.801, -4.200 \pm 0.290, 0.001 \pm 0.001\}$. Note that the above formula does not predict $f_{\Delta\nu} = 1$ for solar properties, since we did not require the formula to pass through the solar reference point. To obtain the most accurate estimations on $f_{\Delta\nu}$, we suggest using the provided Python routine.

Naturally, fitting formula would need to be tested before applying outside the parameter ranges of our sample. Extending it to other ranges, such as metal-poor, high-mass, and red-clump stars, requires more data and will be the subject of future work.

5.2 Comparisons to Gaia radii

To show how the surface corrected $f_{\Delta\nu}$ affects stellar radii, we compared the asteroseismic radii with the Gaia radii calculated by Zinn (2021), using the APOKASC sample (Pinsonneault et al. 2018). The T_{eff} and $[\text{M}/\text{H}]$ from APOGEE (Abdurro’uf et al. 2022) were used to derive Gaia radii for bolometric corrections and converting from luminosities. We calculated the asteroseismic radii through Eq. 15, where we adopted the SYD pipeline values for $\Delta\nu$ and ν_{\max} (Serenelli et al. 2017; Yu et al. 2018), and T_{eff} from APOGEE.

Fig. 9 shows the result. Without the surface correction considered, the $f_{\Delta\nu}$ in this work (blue triangles) produce similar radii to S16 (black circles), despite the fact that the underlying stellar models are different. Christensen-Dalsgaard et al. (2020) reported a spread of only 0.2% in the values of $f_{\Delta\nu}$ from different stellar modelling code. In addition, we found that differences in the mixing length can change $f_{\Delta\nu}$ by $\sim 1\%$ (see Appendix B for more details). A larger discrepancy emerges when we applied the surface correction (red squares). Eq. 15 indicates that the seismic radius is proportional to $f_{\Delta\nu}^2$. Since correctly accounting for the surface effect reduces $f_{\Delta\nu}$ by $\sim 2\%$ for RGB stars (Fig. 8), this translates to a systematic $\sim 4\%$ decrease of the asteroseismic radius scale. This is exactly what we see in Fig. 9. As summarized by Zinn et al. (2019), the systematic uncertainties involved in this comparison, such as uncertainties in bolometric correction and extinction, the IRFM temperature scale, and asteroseismic reference points, can add up to 2%. It is not yet possible to conclude any disagreement between the asteroseismic and Gaia radii with this precision.

There is a significant excursion of red squares at $R > 10 R_{\odot}$ in Fig. 9 that cannot be explained by the causes discussed above. The dip associated with the excursion is also present when using the $f_{\Delta\nu}$ without surface correction. The red clump stars, which burn helium in the core, have radii around $10 R_{\odot}$ (see Fig. 6 of Li et al. 2021a). After exhausting core helium, they become asymptotic-giant-branch (AGB) stars and are difficult to be distinguished from RGB stars based on g-mode period spacings alone (Kallinger et al. 2012; Dréau et al. 2021). Hence, the dip is probably a result of the contamination from AGB stars in the sample. This is supported by the excess of very low-mass stars above $10 R_{\odot}$, due to AGB stars having lost more mass than RGB stars (see Fig. 2g of Li et al. 2021a). The impact of this contamination on Galactic population studies clearly deserves further investigation.

5.3 Comparisons to eclipsing binaries

Similarly, we can compare the asteroseismic radius and mass with the dynamical properties determined from eclipsing binaries. We used the eclipsing binary sample studied by Gaulme et al. (2016), Themeßl et al. (2018), Brogaard et al. (2018) and Benbakoura et al. (2021), who determined the dynamical masses and radii through radial-velocity and lightcurve modelling. We calculated their asteroseismic radii and masses through Eq. 14 and 15, using $\Delta\nu$, ν_{\max} , and T_{eff} reported in Benbakoura et al. (2021). Fig. 10 shows the resulting comparison. Using the corrected $f_{\Delta\nu}$ produces excellent agreement of those properties determined from the two independent means, while the $f_{\Delta\nu}$ without correction tends to systematically overestimate them. Although Benbakoura

et al. (2021) did not consider the surface corrected $f_{\Delta\nu}$, they also found agreement between the asteroseismic and dynamical properties, through modifying the solar reference values appearing in the scaling relations. Our results thus remove the need to shift the reference values when the surface correction is taken into account. Moreover, the impact of surface correction changes as a function of stellar properties (Fig. 8), so it would be difficult to reconcile all stars if the reference values are treated as a constant.

According to Eq. 14, the scaling mass is proportional to $f_{\Delta\nu}^4$ (e.g. Sharma et al. 2016). Hence, as a result of the change in $f_{\Delta\nu}$, the seismic mass scale decreases by $\sim 8\%$. This could have significant consequences for Galactic archaeology since the ages of low-mass stars are critically dependent on their masses.

6 CONCLUSIONS

We provide a prescription for the surface correction as a function of stellar properties, exploiting the fact that the correction should vary smoothly across the H–R diagram. Our main findings are summarised as follows:

(i) The absolute values of the surface correction are larger in main-sequence stars and smaller in RGB stars. For the relative surface correction as a fraction of ν_{\max} , the trend is reversed (Sec. 3.4 and Fig. 3).

(ii) Using the prescription, we were able to reduce scatter and the number of outliers in stellar properties estimated from stellar modelling (Sec. 4 and Figs. 5 and 6). This demonstrates the power of our ensemble-based parameterization of the surface correction.

(iii) We present our stellar models in an online repository. The models include radial frequencies before and after applying the surface correction calibrated in this work.

(iv) Taking into account the surface correction, we present a revised $\Delta\nu$ scaling relation (Sec. 5.1 and Fig. 7). We provided a fitting formula (Eq. 16) and a Python routine to determine $f_{\Delta\nu}$ given user-specified observables.

(v) The values of $f_{\Delta\nu}$ are smaller by up to 2%, after taking into account the surface correction (Sec. 5.1 and Fig. 8). This results in decreases of up to 4% in radii and up to 8% in masses when using the asteroseismic scaling relations.

(vi) We showed that the mass and radius determined with the revised $f_{\Delta\nu}$ improve the agreement with those determined from eclipsing binaries (Sec. 5.3 and Fig. 10).

For most readers, item (iv) will be the most useful. It describes a modification to the $\Delta\nu$ scaling relation that, for the first time, takes the surface correction into account and we encourage its use when deriving masses and radii from asteroseismic parameters.

ACKNOWLEDGEMENTS

We thank Warrick Ball, Sarbani Basu, Karsten Brogaard, Jørgen Christensen-Dalsgaard, and Günter Houdek for interesting comments and discussions. T.R.B acknowledges funding from the Australian Research Council (Discovery Project DP210103119 and Laureate Fellowship FL220100117). D.H.

acknowledges support from the Alfred P. Sloan Foundation and the National Aeronautics and Space Administration (80NSSC19K0597). M.J. acknowledges the Lasker Fellowship granted by the Space Telescope Science Institute. T.L. acknowledges the Joint Research Fund in Astronomy (U2031203) under cooperative agreement between the National Natural Science Foundation of China (NSFC) and Chinese Academy of Sciences (CAS) and the NSFC grants 12090040 and 12090042. H.K. acknowledges funding for the Stellar Astrophysics Centre provided by The Danish National Research Foundation (Grant agreement no.: DNR106).

We gratefully acknowledge the Kepler teams, whose efforts made these results possible. Funding for the Kepler mission is provided by the NASA Science Mission Directorate. This paper includes data collected by the Kepler mission and obtained from the MAST data archive at the Space Telescope Science Institute (STScI). STScI is operated by the Association of Universities for Research in Astronomy, Inc., under NASA contract NAS 5–26555.

This work presents results from the European Space Agency (ESA) space mission Gaia. Gaia data are being processed by the Gaia Data Processing and Analysis Consortium (DPAC). Funding for the DPAC is provided by national institutions, in particular the institutions participating in the Gaia MultiLateral Agreement (MLA). The Gaia mission website is <https://www.cosmos.esa.int/gaia>. The Gaia archive website is <https://archives.esac.esa.int/gaia>.

Funding for the Sloan Digital Sky Survey IV has been provided by the Alfred P. Sloan Foundation, the U.S. Department of Energy Office of Science, and the Participating Institutions.

We acknowledge the use of the National Computational Infrastructure (NCI) which is supported by the Australian Government, and accessed through the Sydney Informatics Hub HPC Allocation Scheme, which is supported by the Deputy Vice-Chancellor (Research), University of Sydney.

This work is made possible by the following open-source software: Numpy (van der Walt et al. 2011), Scipy (Virtanen et al. 2020), Matplotlib (Hunter 2007), Astropy (Astropy Collaboration et al. 2013, 2018), Pandas (Wes McKinney 2010), MESA (Paxton et al. 2011, 2013, 2015, 2018, 2019), GYRE (Townsend & Teitler 2013), ISOCCLASSIFY (Huber et al. 2017; Berger et al. 2020), JAX and OPTAX (Babuschkin et al. 2020), tqdm (da Costa-Luis et al. 2023), tensorflow.

DATA AVAILABILITY

The code and processed data used in this work are available on Github.¹ The calibrated stellar models including oscillation frequencies and the correction factors $f_{\Delta\nu}$ can be downloaded from zenodo.² All raw data (e.g. the Keck spectra) are available on request to the corresponding authors.

REFERENCES

Abdurro'uf et al., 2022, *ApJS*, 259, 35
 Aguirre Børsen-Koch V., et al., 2022, *MNRAS*, 509, 4344

¹ <https://www.github.com/parallelpro/surface>

² <https://zenodo.org/record/7905521>

- Ahumada R., et al., 2020, *ApJS*, **249**, 3
- Asplund M., Grevesse N., Sauval A. J., Scott P., 2009, *ARA&A*, **47**, 481
- Astropy Collaboration et al., 2013, *A&A*, **558**, A33
- Astropy Collaboration et al., 2018, *AJ*, **156**, 123
- Babuschkin I., et al., 2020, The DeepMind JAX Ecosystem, <http://github.com/deepmind>
- Ball W. H., Gizon L., 2014, *A&A*, **568**, A123
- Ball W. H., Gizon L., 2017, *A&A*, **600**, A128
- Balmforth N. J., 1992, *MNRAS*, **255**, 632
- Balona L. A., et al., 2013, *MNRAS*, **430**, 3472
- Basu S., et al., 2011, *ApJ*, **729**, L10
- Bedding T. R., et al., 2011, *Nature*, **471**, 608
- Belkacem K., Kupka F., Philidet J., Samadi R., 2021, *A&A*, **646**, L5
- Bellinger E. P., Angelou G. C., Hekker S., Basu S., Ball W. H., Guggenberger E., 2016, *ApJ*, **830**, 31
- Benbakoura M., et al., 2021, arXiv e-prints, p. [arXiv:2101.05351](https://arxiv.org/abs/2101.05351)
- Berger T. A., Huber D., van Saders J. L., Gaidos E., Tayar J., Kraus A. L., 2020, *AJ*, **159**, 280
- Brewer L. N., et al., 2016, *AJ*, **151**, 66
- Brogaard K., et al., 2012, *A&A*, **543**, A106
- Brogaard K., et al., 2018, *MNRAS*, **476**, 3729
- Brogaard K., Arentoft T., Jessen-Hansen J., Miglio A., 2021, *MNRAS*, **507**, 496
- Broomhall A. M., Chaplin W. J., Davies G. R., Elsworth Y., Fletcher S. T., Hale S. J., Miller B., New R., 2009, *MNRAS*, **396**, L100
- Brown T. M., Gilliland R. L., Noyes R. W., Ramsey L. W., 1991, *ApJ*, **368**, 599
- Buchhave L. A., Latham D. W., 2015, *ApJ*, **808**, 187
- Buchler J. R., Yueh W. R., 1976, *ApJ*, **210**, 440
- Casagrande L., et al., 2021, *MNRAS*, **507**, 2684
- Cassisi S., Potekhin A. Y., Pietrinferni A., Catelan M., Salaris M., 2007, *ApJ*, **661**, 1094
- Choi J., Dotter A., Conroy C., Cantiello M., Paxton B., Johnson B. D., 2016, *ApJ*, **823**, 102
- Christensen-Dalsgaard J., 2012, *Astronomische Nachrichten*, **333**, 914
- Christensen-Dalsgaard J., Dappen W., Lebreton Y., 1988, *Nature*, **336**, 634
- Christensen-Dalsgaard J., Thompson M. J., Gough D. O., 1989, *MNRAS*, **238**, 481
- Christensen-Dalsgaard J., et al., 1996, *Science*, **272**, 1286
- Christensen-Dalsgaard J., et al., 2020, *A&A*, **635**, A165
- Claret A., Torres G., 2018, *ApJ*, **859**, 100
- Compton D. L., Bedding T. R., Ball W. H., Stello D., Huber D., White T. R., Kjeldsen H., 2018, *MNRAS*, **479**, 4416
- Corsaro E., et al., 2012, *ApJ*, **757**, 190
- Cunha M. S., et al., 2021, *MNRAS*, **508**, 5864
- Dréau G., Mosser B., Lebreton Y., Gehan C., Kallinger T., 2021, *A&A*, **650**, A115
- Duan R. M., Zong W., Fu J. N., Chen Y. H., Hermes J. J., Vanderbosch Z. P., Ma X. Y., Charpinet S., 2021, *ApJ*, **922**, 2
- Dziembowski W. A., Paterno L., Ventura R., 1988, *A&A*, **200**, 213
- Eddington A. S., 1926, *The Internal Constitution of the Stars*. The University Press
- El-Badry K., Rix H.-W., Heintz T. M., 2021, *MNRAS*, **506**, 2269
- Elsworth Y., Hekker S., Basu S., Davies G. R., 2017, *MNRAS*, **466**, 3344
- Ferguson J. W., Alexander D. R., Allard F., Barman T., Bodnarik J. G., Hauschildt P. H., Heffner-Wong A., Tamanai A., 2005, *ApJ*, **623**, 585
- Furlan E., et al., 2018, *ApJ*, **861**, 149
- Gaia Collaboration et al., 2016, *A&A*, **595**, A1
- Gaia Collaboration et al., 2021, *A&A*, **649**, A1
- Gaulme P., et al., 2016, *ApJ*, **832**, 121
- Gough D. O., 1990, *Comments on Helioseismic Inference*. Springer-Verlag Berlin Heidelberg, p. 283, [doi:10.1007/3-540-53091-6](https://doi.org/10.1007/3-540-53091-6)
- Green G. M., Schlafly E., Zucker C., Speagle J. S., Finkbeiner D., 2019, *ApJ*, **887**, 93
- Grigahcène A., Dupret M. A., Sousa S. G., Monteiro M. J. P. F. G., Garrido R., Scuflaire R., Gabriel M., 2012, *MNRAS*, **422**, L43
- Grundahl F., et al., 2017, *ApJ*, **836**, 142
- Guggenberger E., Hekker S., Basu S., Bellinger E., 2016, *MNRAS*, **460**, 4277
- Handberg R., Brogaard K., Miglio A., Bossini D., Elsworth Y., Slumstrup D., Davies G. R., Chaplin W. J., 2017, *MNRAS*, **472**, 979
- Hekker S., 2020, *Frontiers in Astronomy and Space Sciences*, **7**, 3
- Heney L., Vardya M. S., Bodenheimer P., 1965, *ApJ*, **142**, 841
- Herwig F., 2000, *A&A*, **360**, 952
- Hon M., Stello D., Yu J., 2017, *MNRAS*, **469**, 4578
- Houdek G., Trampedach R., Aarslev M. J., Christensen-Dalsgaard J., 2017, *MNRAS*, **464**, L124
- Houdek G., Lund M. N., Trampedach R., Christensen-Dalsgaard J., Handberg R., Appourchaux T., 2019, *MNRAS*, **487**, 595
- Howard A. W., et al., 2010, *ApJ*, **721**, 1467
- Huber D., et al., 2011, *ApJ*, **743**, 143
- Huber D., et al., 2017, *ApJ*, **844**, 102
- Hunter J. D., 2007, *Computing in Science & Engineering*, **9**, 90
- Iglesias C. A., Rogers F. J., 1993, *ApJ*, **412**, 752
- Iglesias C. A., Rogers F. J., 1996, *ApJ*, **464**, 943
- Jeffries Mark W. J., et al., 2013, *AJ*, **146**, 58
- Jiang C., Gizon L., 2021, *Research in Astronomy and Astrophysics*, **21**, 226
- Jofré E., Petrucci R., Saffe C., Saker L., Artur de la Villarmois E., Chavero C., Gómez M., Mauas P. J. D., 2015, *A&A*, **574**, A50
- Johnson J. A., et al., 2017, *AJ*, **154**, 108
- Jørgensen A. C. S., Weiss A., Mosumgaard J. R., Silva Aguirre V., Sahlholdt C. L., 2017, *MNRAS*, **472**, 3264
- Jørgensen A. C. S., Mosumgaard J. R., Weiss A., Silva Aguirre V., Christensen-Dalsgaard J., 2018, *MNRAS*, **481**, L35
- Jørgensen A. C. S., Weiss A., Angelou G., Silva Aguirre V., 2019, *MNRAS*, **484**, 5551
- Jørgensen A. C. S., et al., 2020, *MNRAS*, **495**, 4965
- Joyce M., Chaboyer B., 2018a, *ApJ*, **856**, 10
- Joyce M., Chaboyer B., 2018b, *ApJ*, **864**, 99
- Kallinger T., et al., 2010, *A&A*, **509**, A77
- Kallinger T., et al., 2012, *A&A*, **541**, A51
- Kallinger T., Beck P. G., Stello D., Garcia R. A., 2018, *A&A*, **616**, A104
- Kjeldsen H., Bedding T. R., 1995, *A&A*, **293**, 87
- Kjeldsen H., Bedding T. R., Christensen-Dalsgaard J., 2008, *ApJ*, **683**, L175
- Li Y., Bedding T. R., Li T., Bi S., Stello D., Zhou Y., White T. R., 2020a, *MNRAS*, **495**, 2363
- Li T., Bedding T. R., Christensen-Dalsgaard J., Stello D., Li Y., Keen M. A., 2020b, *MNRAS*, **495**, 3431
- Li Y., Bedding T. R., Stello D., Sharma S., Huber D., Murphy S. J., 2021a, *MNRAS*, **501**, 3162
- Li Y., Zhang Q.-s., Wu T., Su J., Chen X.-h., Lin G.-f., Guo J.-h., Liu J.-y., 2021b, *ApJ*, **916**, 107
- Li T., Li Y., Bi S., Bedding T. R., Davies G., Du M., 2022, *ApJ*, **927**, 167
- Lindgren L., et al., 2021, *A&A*, **649**, A4
- Lund M. N., et al., 2017, *ApJ*, **835**, 172
- Lyttle A. J., et al., 2021, *MNRAS*, **505**, 2427
- Magic Z., Weiss A., 2016, *A&A*, **592**, A24
- Maíz Apellániz J., Pantaleoni González M., Barbá R. H., 2021, *A&A*, **649**, A13
- Manchon L., Belkacem K., Samadi R., Sonoi T., Marques J. P. C., Ludwig H. G., Caffau E., 2018, *A&A*, **620**, A107
- McKeever J. M., Basu S., Corsaro E., 2019, *ApJ*, **874**, 180
- Mosser B., et al., 2012, *A&A*, **537**, A30

- Mosser B., et al., 2014, *A&A*, **572**, L5
- Mosumgaard J. R., Jørgensen A. C. S., Weiss A., Silva Aguirre V., Christensen-Dalsgaard J., 2020, *MNRAS*, **491**, 1160
- Nsamba B., Campante T. L., Monteiro M. J. P. F. G., Cunha M. S., Rendle B. M., Reese D. R., Verma K., 2018, *MNRAS*, **477**, 5052
- Ong J. M. J., Basu S., Roxburgh I. W., 2021a, *ApJ*, **920**, 8
- Ong J. M. J., Basu S., Lund M. N., Bieryla A., Viani L. S., Latham D. W., 2021b, *ApJ*, **922**, 18
- Paxton B., Bildsten L., Dotter A., Herwig F., Lesaffre P., Timmes F., 2011, *ApJS*, **192**, 3
- Paxton B., et al., 2013, *ApJS*, **208**, 4
- Paxton B., et al., 2015, *ApJS*, **220**, 15
- Paxton B., et al., 2018, *ApJS*, **234**, 34
- Paxton B., et al., 2019, *ApJS*, **243**, 10
- Petigura E. A., 2015, PhD thesis, University of California, Berkeley
- Petigura E. A., et al., 2017, *AJ*, **154**, 107
- Philidet J., Belkacem K., Goupil M. J., 2021, *A&A*, **656**, A95
- Pinsonneault M. H., et al., 2018, *ApJS*, **239**, 32
- Pols O. R., Tout C. A., Eggleton P. P., Han Z., 1995, *MNRAS*, **274**, 964
- Potekhin A. Y., Chabrier G., 2010, *Contributions to Plasma Physics*, **50**, 82
- Rodrigues T. S., et al., 2017, *MNRAS*, **467**, 1433
- Rogers F. J., Nayfonov A., 2002, *ApJ*, **576**, 1064
- Rosenthal C. S., Christensen-Dalsgaard J., Nordlund Å., Stein R. F., Trampedach R., 1999, *A&A*, **351**, 689
- Sandquist E. L., et al., 2013, *ApJ*, **762**, 58
- Saumon D., Chabrier G., van Horn H. M., 1995, *ApJS*, **99**, 713
- Schmitt J. R., Basu S., 2015, *ApJ*, **808**, 123
- Serenelli A., et al., 2017, *ApJS*, **233**, 23
- Sharma S., Stello D., Bland-Hawthorn J., Huber D., Bedding T. R., 2016, *ApJ*, **822**, 15
- Silva Aguirre V., et al., 2015, *MNRAS*, **452**, 2127
- Sonoi T., Samadi R., Belkacem K., Ludwig H. G., Caffau E., Mosser B., 2015, *A&A*, **583**, A112
- Sonoi T., Ludwig H. G., Dupret M. A., Montalbán J., Samadi R., Belkacem K., Caffau E., Goupil M. J., 2019, *A&A*, **621**, A84
- Stello D., Bruntt H., Preston H., Buzasi D., 2008, *ApJ*, **674**, L53
- Stello D., et al., 2010, *ApJ*, **713**, L182
- Stello D., et al., 2013, *ApJ*, **765**, L41
- Tayar J., et al., 2017, *ApJ*, **840**, 17
- Tayar J., Claytor Z. R., Huber D., van Saders J., 2022, *ApJ*, **927**, 31
- Thiemeßl N., et al., 2018, *MNRAS*, **478**, 4669
- Timmes F. X., Swesty F. D., 2000, *ApJS*, **126**, 501
- Townsend R. H. D., Teitler S. A., 2013, *MNRAS*, **435**, 3406
- Trampedach R., Aarslev M. J., Houdek G., Collet R., Christensen-Dalsgaard J., Stein R. F., Asplund M., 2017, *MNRAS*, **466**, L43
- Ulrich R. K., 1986, *ApJ*, **306**, L37
- Valle G., Dell'Omodarme M., Prada Moroni P. G., Degl'Innocenti S., 2015, *A&A*, **579**, A59
- Vernazza J. E., Avrett E. H., Loeser R., 1981, *ApJS*, **45**, 635
- Virtanen P., et al., 2020, *Nature Methods*, **17**, 261
- Vogt S. S., et al., 1994, in Crawford D. L., Craine E. R., eds, *Society of Photo-Optical Instrumentation Engineers (SPIE) Conference Series Vol. 2198, Instrumentation in Astronomy VIII*. p. 362, doi:10.1117/12.176725
- Vrard M., Mosser B., Samadi R., 2016, *A&A*, **588**, A87
- Wes McKinney 2010, in Stéfan van der Walt Jarrod Millman eds, *Proceedings of the 9th Python in Science Conference*. pp 56 – 61, doi:10.25080/Majora-92bf1922-00a
- White T. R., Bedding T. R., Stello D., Christensen-Dalsgaard J., Huber D., Kjeldsen H., 2011, *ApJ*, **743**, 161
- Yu J., Huber D., Bedding T. R., Stello D., Hon M., Murphy S. J., Khanna S., 2018, *ApJS*, **236**, 42
- Zinn J. C., 2021, *AJ*, **161**, 214
- Zinn J. C., Pinsonneault M. H., Huber D., Stello D., Stassun K., Serenelli A., 2019, *ApJ*, **885**, 166
- da Costa-Luis C., et al., 2023, tqdm: A fast, Extensible Progress Bar for Python and CLI, doi:10.5281/zenodo.7697295, https://doi.org/10.5281/zenodo.7697295
- van der Walt S., Colbert S. C., Varoquaux G., 2011, *Computing in Science and Engineering*, **13**, 22

APPENDIX A: SURFACE CORRECTION WITH HOPF ATMOSPHERIC MODELS

We carried out an additional set of stellar model calculation using the solar-calibrated Hopf atmosphere (Paxton et al. 2013), which is equivalent to the fit provided by Sonoi et al. (2019) to the VAL-C model (Vernazza et al. 1981). The results are presented in Table A1. Notably, there is a significant discrepancy in the fitted coefficients between the pre-*RGB* and *RGB* samples — especially for a , which represents the amount of surface correction at ν_{\max} for a solar model. Considering the atmosphere is solar-calibrated, it may generalise poorly on *RGB* stars. Further studies are needed to understand its cause. To enhance the applicability of the surface correction prescription proposed in this paper, we recommend using the atmosphere calculated based on the Eddington $T-\tau$ relation rather the Hopf atmosphere.

APPENDIX B: SYSTEMATIC UNCERTAINTIES OF THE CORRECTION FACTORS

We can study two types of uncertainties arising from the calculation of the correction factor $f_{\Delta\nu}$. The first type of error is due to uncertain stellar physics. Using our surface-corrected stellar models, we can quantify the spread of $f_{\Delta\nu}$ due to the changes of Y_{init} and α_{MLT} , both of which are poorly constrained model parameters. We generated synthetic stars with the following stellar properties: L , ν_{\max} , T_{eff} , and $[M/H]$, along a $1 M_{\odot}$, solar metallicity, pre-*RGB*-tip evolutionary track from MIST. We assumed 2% observational uncertainties for L , 2% for ν_{\max} , 2.4% for T_{eff} , and 0.1 dex for $[M/H]$, according to their typical values (e.g. Tayar et al. 2022; Yu et al. 2018). Then we treated these properties as observational constraints and estimated $f_{\Delta\nu}$, using the fitting routine introduced in Sec. 5.1. In addition, we assigned Gaussian priors on each model based on its Y_{init} and α_{MLT} values, the results of which are shown in the top and middle panels of Fig. B1. Changing α_{MLT} clearly has a bigger impact than Y_{init} . The differences on the *RGB* and the main sequence are smaller than 0.5%, and in the subgiant phase ($\nu_{\max} \sim 1000 \mu\text{Hz}$) they can reach $\sim 1\%$. However, the $f_{\Delta\nu}$ itself presents a larger variation than these at most $\sim 1\%$ uncertainties (see also Fig. 7), indicating the necessity of making the correction to the $\Delta\nu$ scaling relation.

The second type of error concerns the range of modes that are used to calculate the theoretical $\Delta\nu$. We compared two approaches: one using the default range of modes involved in our work, which is $\nu_{\max} \pm 5\sigma$, and another only using the modes in the $\nu_{\max} \pm 3\Delta\nu$ range. From the bottom panel of Fig. B1, we see negligible differences, indicating that the range of modes considered (as long as larger than $3\Delta\nu$) is not a major source of uncertainty.

Table A1. Best-fitting parameters in the surface correction prescriptions. The stellar models are calculated with $T - \tau$ integrated model atmospheres using the solar-calibrated Hopf relation.

Atmosphere Model	Sample	a	b	c	d	a'	b'	c'	d'
Hopf	Cubic All	-3.06 ± 0.10	0.96 ± 0.01	-7.14 ± 0.20	-0.88 ± 0.02	—	—	—	—
Hopf	Cubic Pre-RGB	-4.25 ± 0.28	0.50 ± 0.06	-0.98 ± 0.49	-0.49 ± 0.08	—	—	—	—
Hopf	Cubic RGB	-2.90 ± 0.10	0.97 ± 0.01	-7.68 ± 0.22	-0.91 ± 0.02	—	—	—	—
Hopf	Inverse-cubic All	-4.73 ± 0.40	0.45 ± 0.06	2.27 ± 0.43	0.66 ± 0.11	-6.01 ± 0.38	-6.01 ± 0.38	-6.01 ± 0.38	-6.01 ± 0.38
Hopf	Inverse-cubic Pre-RGB	-4.73 ± 0.40	0.45 ± 0.06	2.27 ± 0.43	0.66 ± 0.11	-6.01 ± 0.38	-6.01 ± 0.38	-6.01 ± 0.38	-6.01 ± 0.38
Hopf	Inverse-cubic RGB	-1.45 ± 0.03	0.88 ± 0.01	-10.16 ± 0.20	-0.31 ± 0.02	-2.31 ± 0.06	-2.31 ± 0.06	-2.31 ± 0.06	-2.31 ± 0.06

This paper has been typeset from a \LaTeX file prepared by the author.

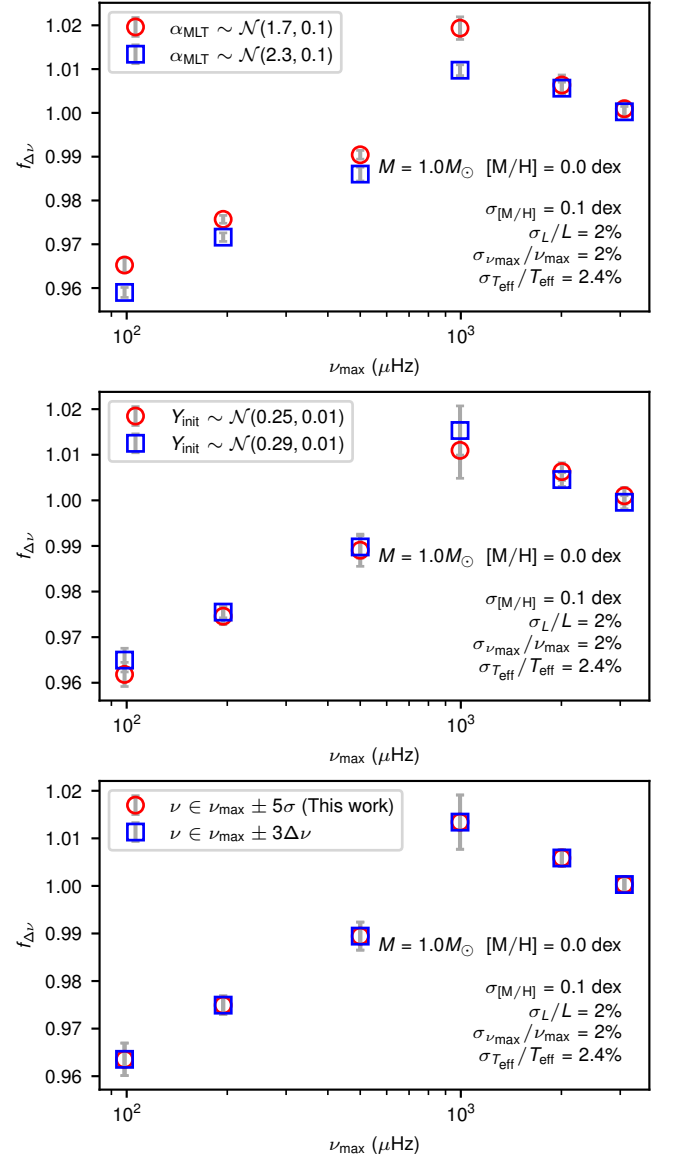


Figure B1. Changes of theoretical $f_{\Delta\nu}$ due to the choices of priors on α_{MLT} and Y_{init} (top and middle panels) and the ranges of modes to be included when calculating model $\Delta\nu$ (bottom panel).